
01 Jan 2023

Effect of Annealing Time on Texture Evolution of Fe–3.4 Wt% Si Nonoriented Electrical Steel

Yizhou Du

Ronald J. O'Malley

Missouri University of Science and Technology, omalleyr@mst.edu

Mario F. Buchely

Missouri University of Science and Technology, buchelym@mst.edu

Paul Kelly

Follow this and additional works at: https://scholarsmine.mst.edu/matsci_eng_facwork

 Part of the [Materials Science and Engineering Commons](#)

Recommended Citation

Y. Du et al., "Effect of Annealing Time on Texture Evolution of Fe–3.4 Wt% Si Nonoriented Electrical Steel," *Steel Research International*, Wiley, Jan 2023.

The definitive version is available at <https://doi.org/10.1002/srin.202300218>

This Article - Journal is brought to you for free and open access by Scholars' Mine. It has been accepted for inclusion in Materials Science and Engineering Faculty Research & Creative Works by an authorized administrator of Scholars' Mine. This work is protected by U. S. Copyright Law. Unauthorized use including reproduction for redistribution requires the permission of the copyright holder. For more information, please contact scholarsmine@mst.edu.

Effect of Annealing Time on Texture Evolution of Fe–3.4 wt% Si Nonoriented Electrical Steel

Yizhou Du,* Ronald J. O'Malley, Mario F. Buchely, and Paul Kelly

Herein, the effect of annealing time on the texture evolution in Fe–3.4 wt% Si non-oriented electrical steel is investigated. Strip samples are cast using a vacuum sampling method, which simulate the solidification conditions of an industrial twin roll thin strip casting (TRSC) process. As-cast samples with different carbon and sulfur (C&S) levels are hot rolled (HR) with varying levels of hot deformation, cold rolled (CR) to 0.35 mm thickness, and then annealed at 1050 °C for different holding times (1, 6, 24 h). To Fe–3.4 wt% Si nonoriented electrical steel, the observed texture evolution can be divided into different stages as annealing time is increased from 1 to 24 h. With increasing annealing time, the fraction of Goss texture decreases initially and then increases again through the consumption of grains with other textures. With additional time, a decrease of pinning force due to precipitate coarsening results in normal grain growth, resulting in an increase of grain size. In this step, Cube grains can form from rotated Goss grains. A model for core loss is presented and used to explain the core loss results.

1. Introduction

As one of the widely used soft magnetic materials, electrical steel can be classified into two classes: nongrain-oriented (NGO) and grain-oriented (GO) electrical steels. GO electrical steel is used in large transformers, while the NGO electrical steel is used in the electric motors and other devices. Based on the desire for high-torque and high-speed electric motors, the NGO electrical steels with low core loss and high magnetic induction^[1,2] are required to achieve these objectives while also achieving high-energy efficiency.

When used in an electrical motor, NGO electrical steel is cut to thin laminations that are isolated with insulating coating layers

and stacked to form the motor core to decrease eddy current losses. Thus, if thin-strip NGO electrical steel can be continuously cast directly to a thin strip, that will be helpful to save the energy and time. In this case, the twin roll thin-strip casting (TRSC) process has excellent potential because it can directly and continuously cast 2 mm-thick steel strips.^[3,4]

When NGO electrical steel is cast by the conventional thick slab continuous casting method, it is difficult to maintain the θ -fiber texture which is always formed in the hot rolled (HR) process.^[5] During the cold rolled (CR) and annealing process, strong α -fiber and γ -fiber textures are commonly observed.^[6] The formation of deformed matrix shear bands directly influenced the nucleation and growth of Goss grains in the recrystallization annealing

process.^[7] Furthermore, because of the low local dislocation density, the retained Goss grains after CR can also promote the formation of Goss grains in the recrystallization annealing process.^[8]

Due to the high solidification cooling rate, the precipitate size distribution on the direct twin-roll cast strip is different from the size distribution observed in the traditional thick slab continuous casting method.^[9] With the high solidification cooling rate of the TRSC process, small precipitates are formed which directly influence the grain growth and texture evolution in the annealing process.^[9] Thus, it is worthwhile to study the influence of the annealing time on the texture evolution for NGO silicon steels produced by the TRSC process.

In this study, a vacuum-assistant fast cooling sampling method was used to produce Fe–3.4 wt% Si NGO electrical steel thin-strip samples that simulate the solidification conditions in the industrial TRSC process. The influence of annealing time at 1050 °C on the texture evolution of the processed strip was investigated.

2. Experimental Section


2.1. Materials

Nonoriented electrical steel samples with different carbon and sulfur (C&S) contents were studied. The chemical compositions are shown in **Table 1**. To control the influence of MnS precipitates and the α -to- γ phase transformation during the annealing process, the low-C&S chemical composition is commonly employed in industry. Steel charges were melted in a 90 kg coreless medium-frequency induction furnace with an Ar protective

Y. Du, R. J. O'Malley, M. F. Buchely
Department of Materials Science and Engineering
Missouri S&T
1400 N Bishop Avenue, Rolla 65409-034, MO, USA
E-mail: yd3t2@mst.edu

P. Kelly
Consultant Castrip LLC
Castrip LLC
1915 Rexford Rd, Suite 150, Charlotte 28211, NC, USA

Y. Du
MCC Capital Engineering & Research Incorporation Limited
No. 7 Jianan jie, Beijing Economic-Technological Development Area,
Beijing 100176, China

 The ORCID identification number(s) for the author(s) of this article can be found under <https://doi.org/10.1002/srin.202300218>.

DOI: 10.1002/srin.202300218

Table 1. Chemical composition of the studied Si steels (wt%).

Steels	C	Si	Mn	Al	S	P
1. Low C&S	0.0046	3.45	1.50	0.001	0.0038	0.008
2. High C&S	0.0098	3.44	1.48	0.002	0.0087	0.010

atmosphere. Using a vacuum sampler, samples were taken directly from the furnace at 100 °C superheat. Details of the sampling procedure have been reviewed previously.^[10]

2.2. Experimental Procedures

In this study, samples were taken using a vacuum assistant fast cooling (VA) sampling method. As shown in **Figure 1**, a vacuum-assisted process was used to draw liquid steel into a thin internal cavity inside the copper mold with high solidification cooling rate. This method can produce a uniform 2 mm-thick strip sample with proper dendrite structure. The solidification cooling rate was calculated at ($\approx 1700^\circ \text{K s}^{-1}$), which simulated the solidification conditions of the TRSC process.^[3,9,10]

After solidification, as shown in **Figure 2**, the 2 mm-thick as-cast samples were hot rolled (HR) with different deformation (0%, 25%, 47%), cold rolled (CR) to 0.35 mm, and batch annealed at 1050 °C for varied times (1, 6, 24 h). This thermomechanical processing routes were designed to simulate an industrial TRSC NGO electrical steel production process.

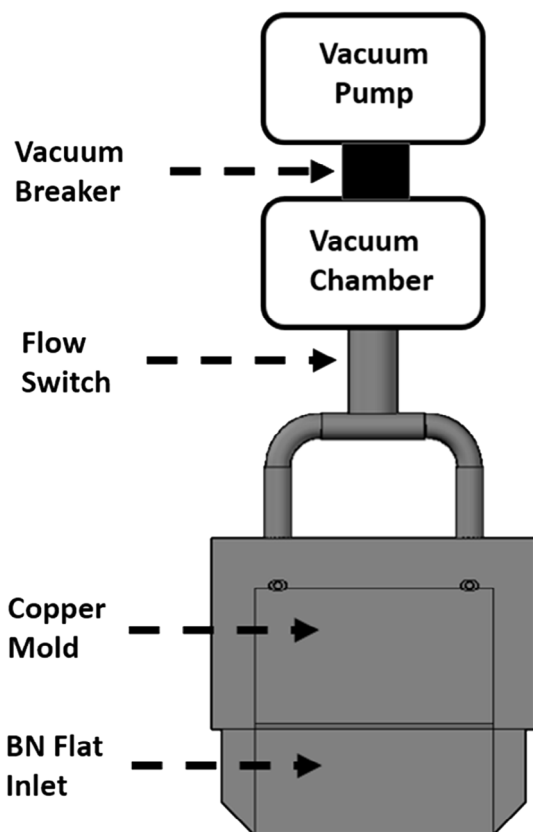


Figure 1. Schematic diagram of VA fast cooling sampler.

For the NGO electrical steel used in this study (0.35 mm thick, $4.70 \times 10^{-7} \Omega \text{ m}$), to minimize the core loss at 1.5 T and 50 Hz condition ($P_{1.5/50}$), the optimum grain size was calculated using the method reported in a previous study.^[9]

Grain size, precipitate size distribution, magnetic properties, and texture distribution of samples with different annealing times were analyzed. The linear intercept method from ASTM E112-13 was used to measure the average grain size, a single-sheet tester was used to measure the magnetic properties, the automated feature analysis (AFA) on ASPEX PICA 1020 SEM was used in precipitates analysis, and the electron backscatter diffraction (EBSD) analysis on Helios SEM equipment was used in analyzing texture distribution. Test samples for magnetic properties were cut along the rolling direction by $100 \times 30 \text{ mm}$ size. EBSD analyses were scanned along the rolling direction–normal direction planes (RD–ND) cross section. The harmonic series expansion method was used in the orientation distribution function (ODF) calculations.

3. Results and Discussion

3.1. Grain Size Effect

The grain growth condition after batch annealing at 1050 °C for various hold times is shown in **Figure 3**. It can also be observed that the growth rates are higher in the first 6 h of batch annealing and slows in the 6–24 h time range. This phenomenon was observed in every sample under each condition.

The calculated optimum grain size is $\approx 250 \mu\text{m}$, which is larger than all the measured average grain sizes in this study. Thus, the larger grain size will be more beneficial in decreasing core loss $P_{1.5/50}$.

The recrystallization and grain growth in annealing process can be inhibited by the pinning effect of these precipitates on the grain boundaries.

Zener and Smith^[11] described the pinning force by small precipitates as follows.

$$Z_p = \frac{3\gamma_{GB}F_v}{2r} \quad (1)$$

where γ_{GB} is the grain boundary energy, F_v is the precipitate volume fraction, and r is the precipitate average radius.

Initially, the pinning force is higher than the driving force for the recrystallization and grain growth. Then, as shown in **Figure 4**, precipitates coarsen during the annealing process, which gives fewer small precipitates ($< 0.85 \mu\text{m}$) and more large precipitates ($> 0.85 \mu\text{m}$) after final annealing. According to Equation (1), the larger precipitates have a lower pinning force, which reduces the grain boundary pinning effect.

3.2. Magnetic Properties

The magnetic properties of different HR deformation 1050 °C batch-annealed samples are shown in **Table 2**. It can be observed from **Table 2** that the magnetic properties are highly influenced by the average grain size. As shown in **Table 2**, with the low-C&S 25% HR that has been batch annealed at 1050 °C from 1 to 24 h,

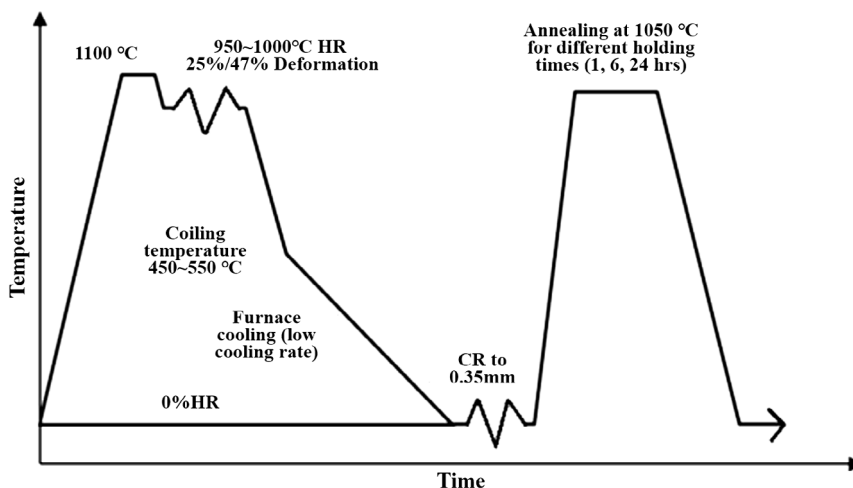


Figure 2. Schematic diagram of thermomechanical processing route.

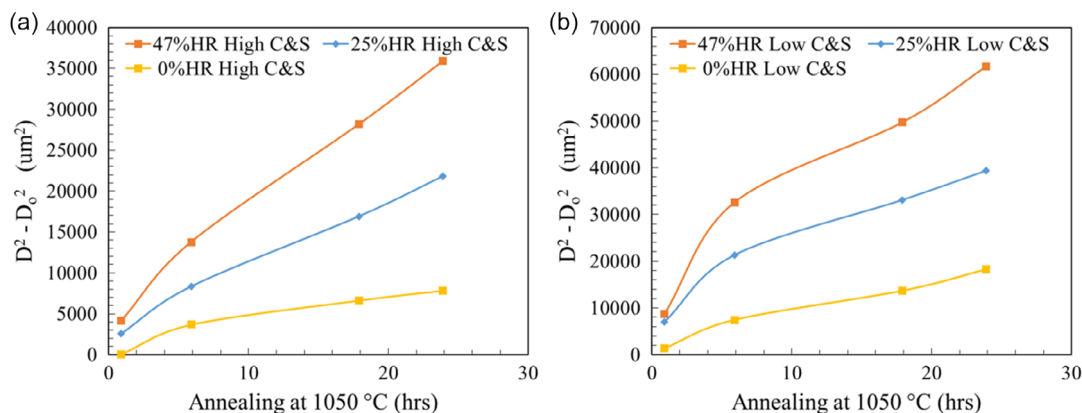


Figure 3. $D^2 - D_0^2$ versus batch annealing time at 1050 °C for a) high C&S sample and b) low C&S sample.

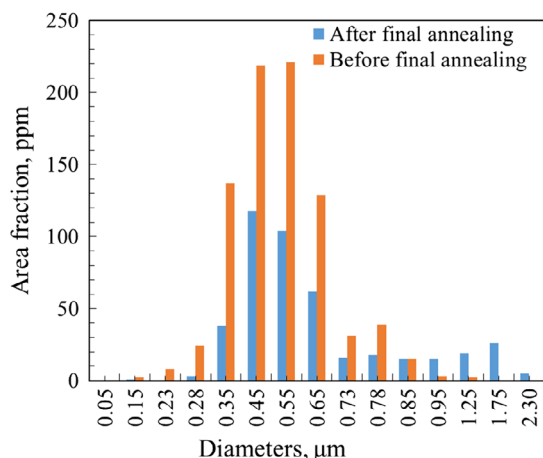


Figure 4. Precipitate size distribution about equivalent diameter versus Area fraction (total particle area/total scan area) of low C&S 25% HR sample before and after final annealing (1050 °C 24 h).

Table 2. Magnetic properties after 1050 °C batch annealing.

	$P_{1.5/50}$ [W kg ⁻¹]	B_{25} [mT]	Average grain size [µm]
High C&S 0% HR (24 h)	2.900	1672	89 ± 3
High C&S 25% HR (24 h)	2.380	1860	148 ± 6
High C&S 47% HR (24 h)	2.267	1970	190 ± 8
Low C&S 0% HR (24 h)	2.790	1786	136 ± 5
Low C&S 25% HR (1 h)	2.853	1609	86 ± 2
Low C&S 25% HR (6 h)	2.814	1704	147 ± 6
Low C&S 25% HR (24 h)	2.380	1910	199 ± 9
Low C&S 47% HR (1 h)	2.826	1638	95 ± 3
Low C&S 47% HR (6 h)	2.808	1763	181 ± 8
Low C&S 47% HR (24 h)	2.020	1990	249 ± 11

the core loss $P_{1.5/50}$ decreased from 2.853 to 2.380 W kg⁻¹, and the magnetic induction B_{25} increased from 1609 to 1910 mT.

3.3. Texture Evolution Texture Components

The position of typical orientations and fiber texture locations for NGO electrical steel on an ODF image is shown in **Figure 5**. From **Figure 6** to **Figure 11**, the ODF images are displayed at $\varphi_2 = 0^\circ$ and 45° sections for samples that were batch annealed at 1050 °C for 1, 6, 24 h.

Figure 6, 8, and 10 show ODF images of the high-C&S steel, while **Figure 7, 9, and 11** show the images for low-C&S steel.

In addition, **Figure 6 and 7** show ODF images for the 0% HR samples, **Figure 8 and 9** show ODF images for the 25% HR samples, and **Figure 10 and 11** show ODF images for the 47% HR samples. The variations of the main texture volume fractions as a function of annealing time are shown in **Figure 12**.

For the high-C&S 0% HR samples (**Figure 6**), nonuniform α -fiber ($\langle 110 \rangle // \text{rolling direction [RD]}$) and α^* -fiber ($\{hhl\} \langle \frac{h}{l} + 1 \frac{h}{l} + 2 \frac{h}{l} \rangle$) textures can be observed after 1 h of annealing. After 6 h of annealing, nonuniform α^* -fiber texture can still be observed, while the α -fiber texture has already disappeared. After 24 h annealing, the α^* -fiber texture has also disappeared.

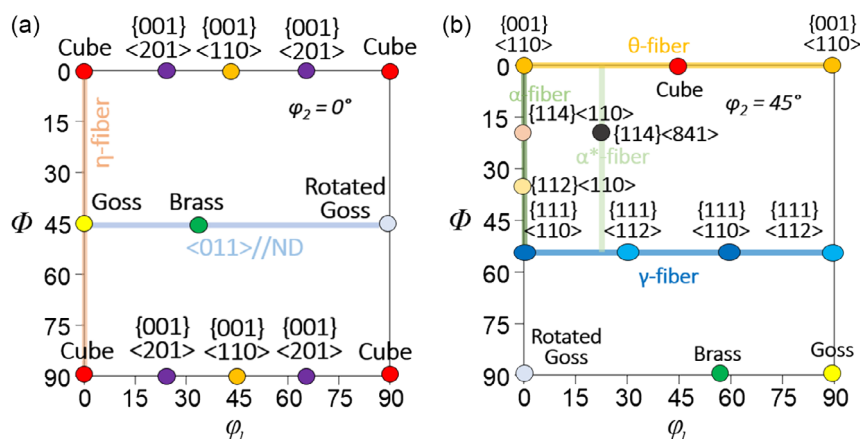


Figure 5. Electrical steel typical texture components on ODF image: a) $\varphi_2 = 0^\circ$, and b) $\varphi_2 = 45^\circ$ section.

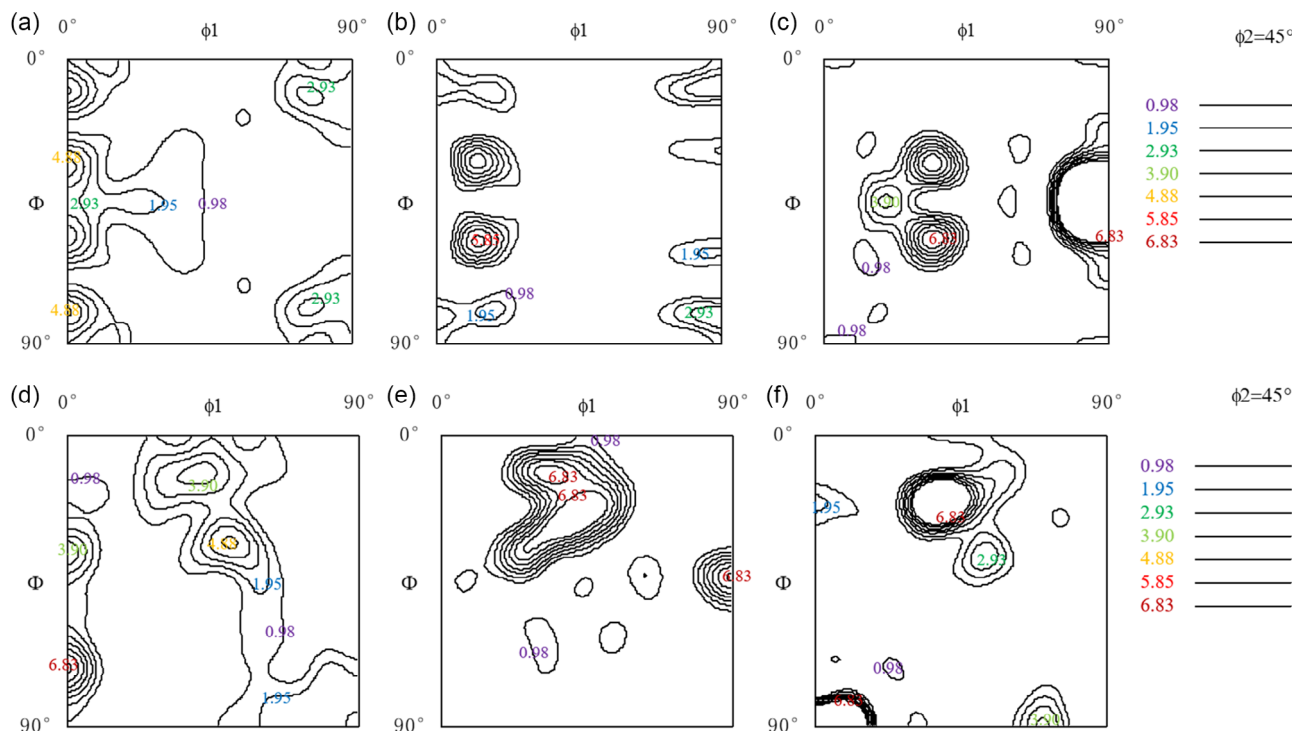


Figure 6. ODF map of the high-C&S VA sample 0% HR, CR to 0.35 mm, and annealed at 1050 °C for a) 1 h, b) 6 h, c) 24 h displayed at $\varphi_2 = 0^\circ$ section; and for d) 1 h, e) 6 h, f) 24 h displayed at $\varphi_2 = 45^\circ$ section.

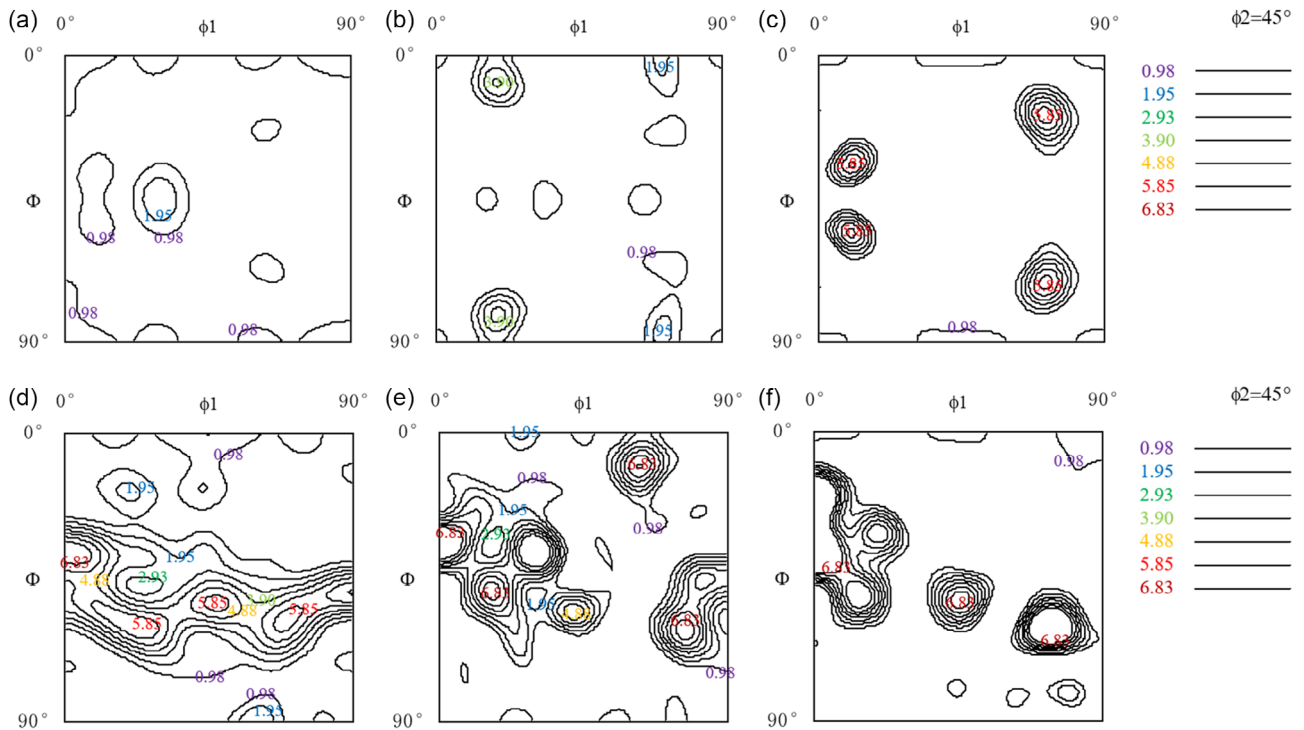


Figure 7. ODF map of the low-C&S VA sample 0% HR, CR to 0.35 mm, and annealed at 1050 °C for a) 1 h, b) 6 h, c) 24 h displayed at $\varphi_2 = 0^\circ$ section and for d) 1 h, e) 6 h, f) 24 h displayed at $\varphi_2 = 45^\circ$ section.

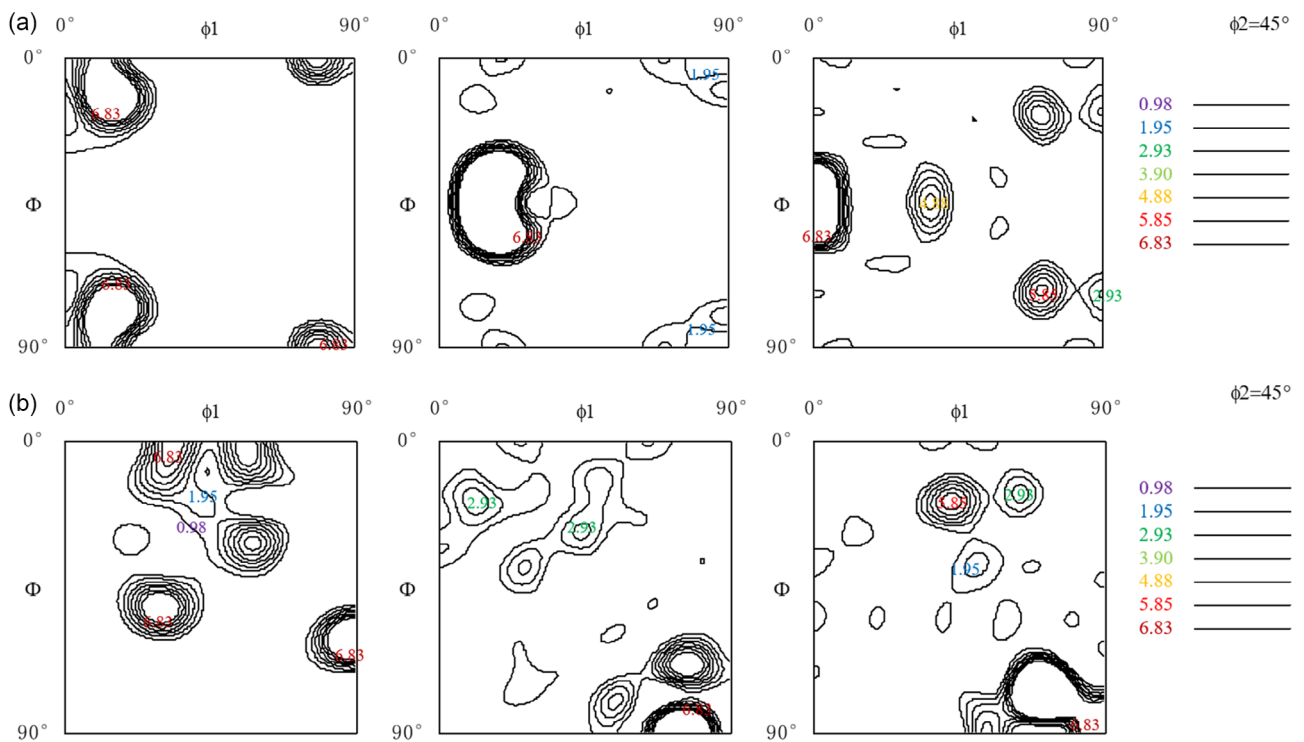


Figure 8. ODF map of the high-C&S VA sample 25% HR, CR to 0.35 mm, and annealed at 1050 °C for a) 1 h, b) 6 h, c) 24 h displayed at $\varphi_2 = 0^\circ$ section; and for d) 1 h, e) 6 h, f) 24 h displayed at $\varphi_2 = 45^\circ$ section.

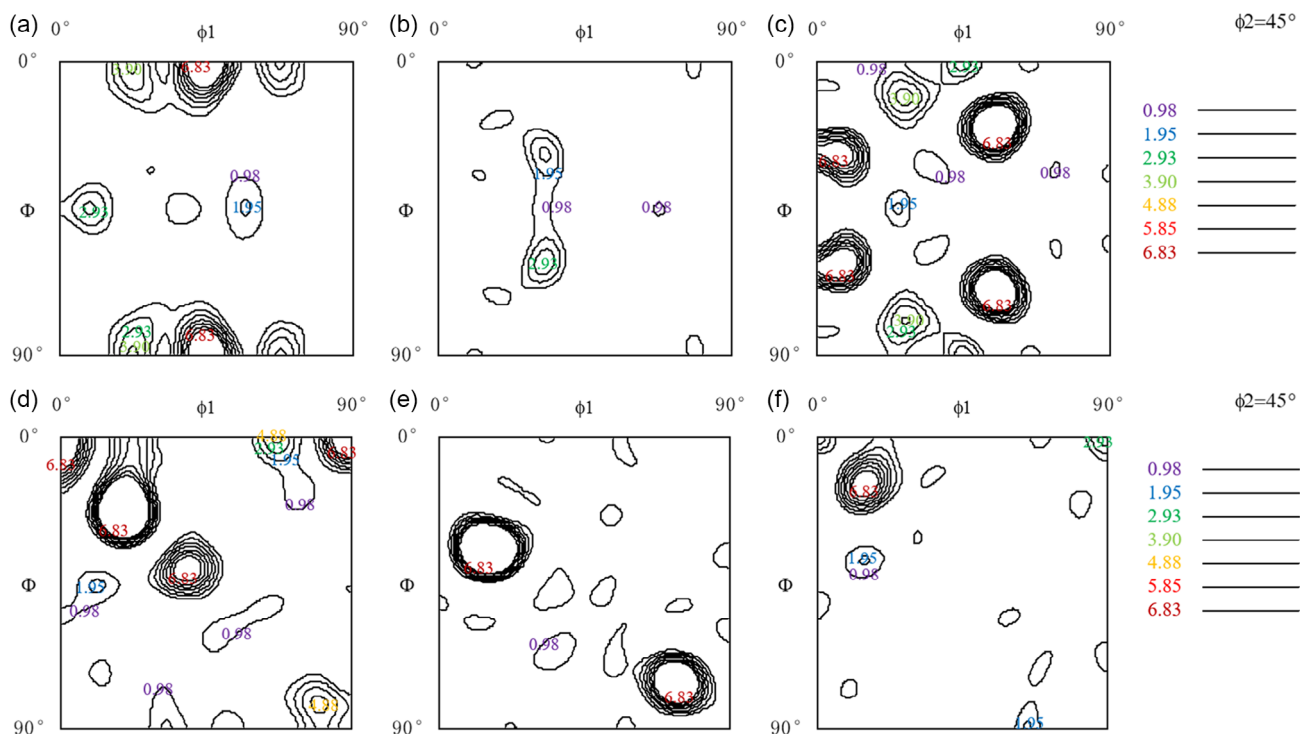


Figure 9. ODF map of the low-C&S VA sample 25% HR, CR to 0.35 mm, and annealed at 1050 °C for a) 1 h, b) 6 h, c) 24 h displayed at $\varphi_2 = 0^\circ$ section; and for d) 1 h, e) 6 h, f) 24 h displayed at $\varphi_2 = 45^\circ$ section.

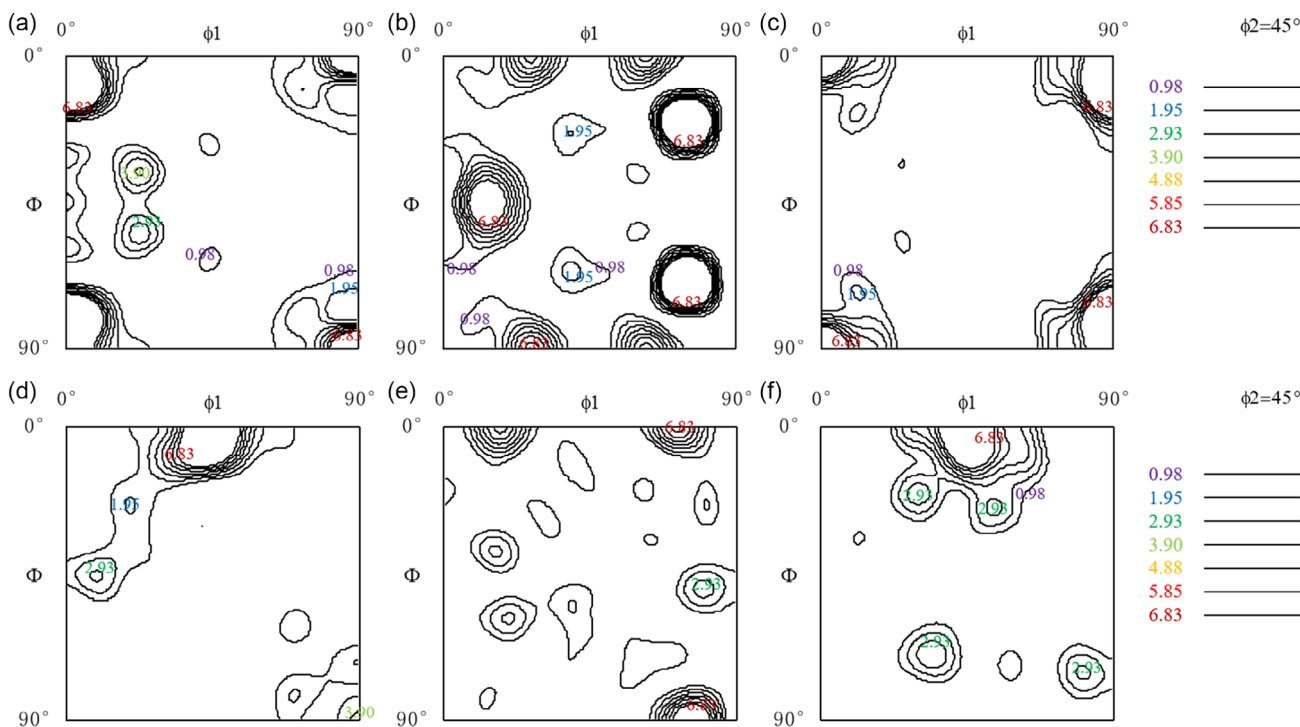


Figure 10. ODF map of the high-C&S VA sample 47% HR, CR to 0.35 mm, and annealed at 1050 °C for a) 1 h, b) 6 h, c) 24 h displayed at $\varphi_2 = 0^\circ$ section; and for d) 1 h, e) 6 h, f) 24 h displayed at $\varphi_2 = 45^\circ$ section.

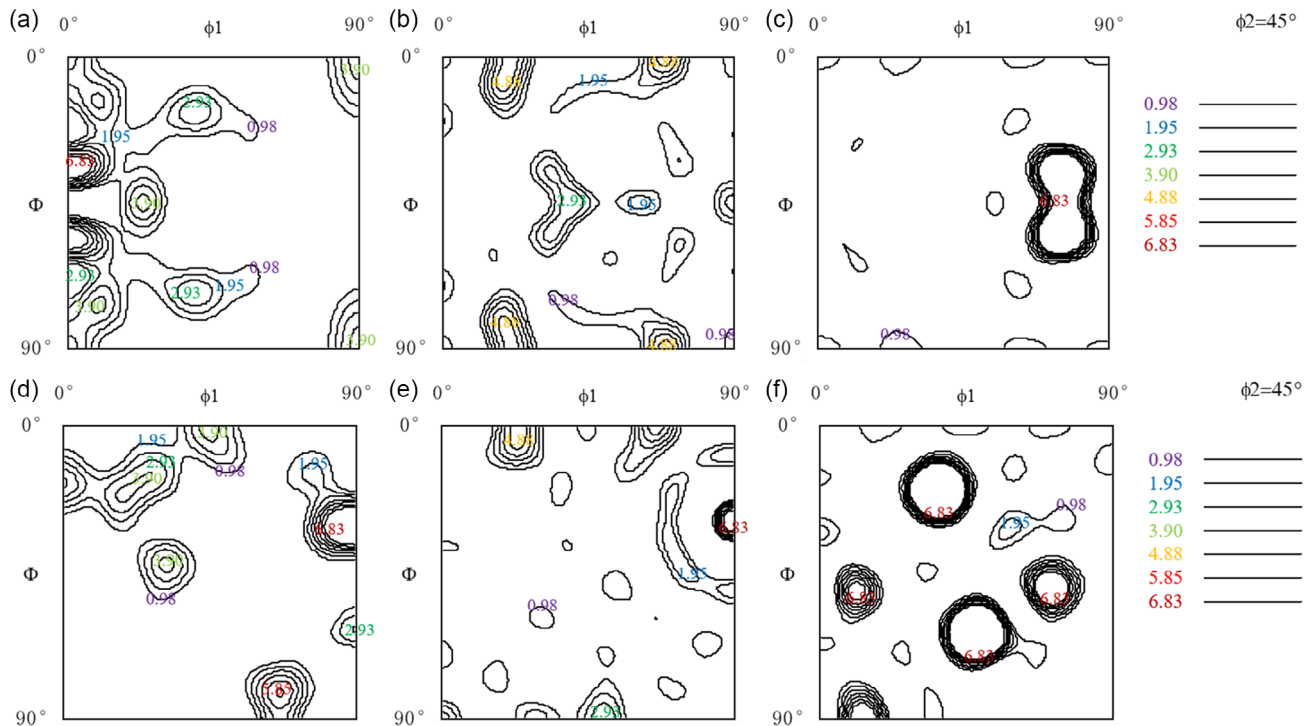


Figure 11. ODF map of the low-C&S VA sample 47% HR, CR to 0.35 mm, and annealed at 1050 °C for a) 1 h, b) 6 h, c) 24 h displayed at $\varphi_2 = 0^\circ$ section; and for d) 1 h, e) 6 h, f) 24 h displayed at $\varphi_2 = 45^\circ$ section.

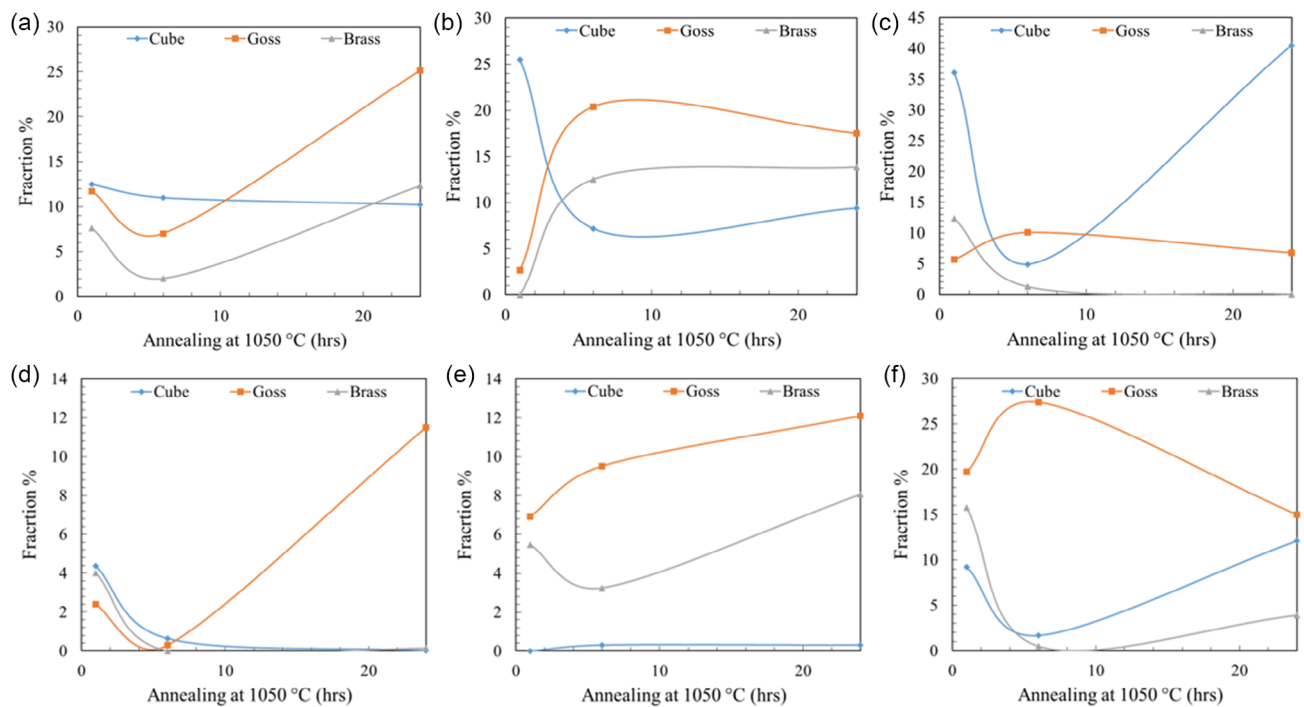


Figure 12. Volume fractions of the main textures versus annealing time to the high-C&S VA sample with a) 0% HR, b) 25% HR, c) 47% HR, and the low-C&S VA sample with d) 0% HR, e) 25% HR, f) 47% HR.

As a comparison, the low-C&S 0% HR samples (Figure 7) are highly influenced by the γ -fiber ($\langle 111 \rangle$ //ND) texture formed before the annealing process. High-intensity γ -fiber texture

and weak nonuniform α^* -fiber texture are observed after 1 h of annealing. After 6 h of annealing, high-intensity γ -fiber texture can still be observed, but it becomes nonuniform. After 24 h, the

high-intensity γ -fiber texture becomes more nonuniform. The nonuniform α^* -fiber texture can be observed after 6 and 24 h.

This phenomenon can be explained by fiber texture evolution. The 0% HR samples were highly influenced by the α^* -fiber and γ -fiber textures which formed before the annealing process. The formation of α^* -fiber and γ -fiber textures is related to the high CR deformation and strain for the 0% HR sample. In the CR process, with the increase of deformation and strain, rotated Goss orientation will gradually rotate to $\{111\}\langle 110\rangle$ orientation and then form the γ -fiber texture.^[12] Finally, with the further increase of deformation and strain, α -fiber and α^* -fiber textures will appear.^[13]

The main texture volume fraction of the 0% HR samples (Figure 12a,d) mostly decreased between 1 and 6 h of annealing time. Between 6 and 24 h, the volume fraction of the Goss orientation increases significantly, while the fractions of other main orientations remain largely unchanged. The main difference is that, compared to the low-C&S sample, the high-C&S samples' Brass orientation volume fraction also increases between 6 and 24 h.

Theories for the thermodynamic driving force for grain growth and critical radius are helpful in explaining the texture evolution.^[14,15] Critical radius can be described as follows.

$$R_c = -\frac{2\gamma}{\Delta G_v} \quad (2)$$

where γ is the boundary energy, and ΔG_v is the driving force. the velocity of grain boundary can be described as follows

$$v = M\gamma \frac{2}{R} \quad (3)$$

where γ is the boundary energy, R is radius, and M is grain boundary mobility (which depends on orientation of adjacent grains).

The texture evolution in Figure 6 and 7 can be divided into two steps. In the first step, the decrease in the volume fraction of Goss grains can be explained by the boundary energy differences between grains. High-energy boundaries are more likely to appear around Goss grain.^[16] Thus, to reduce the system's total energy, it is energetically favorable to consume Goss grains early in the process of grain growth. This phenomenon can also be explained by critical radius difference. In the initial step, a large number of grains smaller than critical radius are consumed. According to Equation (2), higher boundary energy also assigns a larger critical radius to Goss grain. As Hayakawa, Y. reported,^[16] the critical radius of Goss grains is about 9% higher than grains with other textures. Thus, more Goss grains are consumed in the initial step. Furthermore, this phenomenon can also be explained considering the pinning effect of precipitates. At the first step, according to Equation (1) and (3), the pinning force from precipitates is still high and only grains with high-energy boundaries can move.

Then, in the second step, with the precipitates coarsening at longer annealing times, the pinning force is decreased according to Equation (1). In this condition, pinning provides a mobility advantage to the survived Goss grains which are larger than the critical size. As indicated in Equation (3), this mobility advantage results in faster Goss grain growth by consuming other grains which are smaller than the critical size.

Furthermore, this main texture evolution is also related to the evolution of the α^* -fiber and γ -fiber texture. With the longtime annealing, fiber textures nucleated and grew into other texture orientations. Goss orientation on body-centered cubic (BCC) metals has been reported to be more likely to form from the shear deformation orientation and deformed fiber textures.^[17]

For the 25% HR samples (Figure 8 and 9), high-intensity α^* -fiber and γ -fiber textures have not been observed. To the main texture volume fraction in the high-C&S 25% HR sample (Figure 12b), the fraction of Goss and Brass texture grains increased significantly, while the fraction of Cube texture grains decreased significantly between 1 and 6 h. Then, between 6 and 24 h, the fraction of Goss texture grains gradually decreased as the fraction of Cube texture grains increased. For the low-C&S 25% HR sample (Figure 12e), the fraction of Goss texture grains gradually increased between 1 and 24 h, while the fraction of Cube texture grains gradually decreased between 6 and 24 h.

The volume fraction of Cube grains at 1 h can be considered to be influenced by the presence of Cube grains formed before the annealing process. In some cases, Cube texture components were retained after heavy cold rolling because deformed Cube grains serve as nucleation sites for new Cube grains.^[18,19] For the 1–6 h, high-C&S sample (Figure 12b) and the 1–24 h, low-C&S sample, Figure 12e, the increase in the fraction of Goss grains can be explained by the second step, which is caused by a decrease of pinning force giving a boundary mobility advantage to large Goss grains. Finally, with a further decrease of the pinning force and an increase of Goss grains, the mobility advantage becomes similar for all grains.^[16] At this point, selective growth of the Goss grains stops and normal grain growth is established.

For the 47% HR samples (Figure 10 and 11), high-intensity α^* -fiber and γ -fiber textures have also not been observed. For the 47% HR sample (Figure 12b,d) between 1 and 6 h, the fraction of Goss texture grains increased, and the fraction of Cube texture grains decreased significantly. Between 6 and 24 h, the fraction of Goss grains decreased with the sharp increase in the fraction of Cube grains.

In this case, the reversal in the fractions of Goss and Cube grains is related to high volume fraction change in the final step (6–24 h) and is considered to be caused by the formation of Cube grain from rotated Goss grains. Nguyen-Minh et al. reported the crystal volumes or crystallites of Cube orientation formed from the shear band of rotated Goss orientation.^[13,20] It is also reported that, with the increase of strain, the Cube orientation is the most stable orientation formed from the shear bands of rotated Goss grains.^[20]

3.4. Model for Core Loss

Core loss is influenced both by the grain size and by texture distribution. It is difficult to separate their individual contributions to core loss. A qualitative model and equation for predicting core loss would be helpful to separate the contribution of grain size and texture distribution contributions to core loss.

For grain size influence on core loss, Wang Jiayi et al. reported that influence by grain size can be formulated as follows.^[21]

$$P_G = A + Bd^{-1} + Cd^{-2} \quad (4)$$

where d is the average grain size, A to C are positive constants depending on the chemical composition, precipitate size distribution, and test conditions.

According to the model, A represents the energy loss caused by eddy current and domain magnetic direction rotation in each single grain. It is influenced by chemical composition. Bd^{-1} is the energy loss when the domain wall migrates inside the grain. This energy loss is influenced by grain size and precipitate size distribution.^[9] Cd^{-2} represents the energy loss when eddy current passes through the grain boundaries. In practice, this energy loss is very small, because it is difficult for a domain wall to pass through a grain boundary.

For the influence by the texture distribution, Goss and Cube textures provide the main benefit to the magnetic properties. We assume that this effect is linear. The equation for the texture distribution influence is

$$P_T = DF_C + EF_G \quad (5)$$

where D to E are constant, F_C and F_G are the percent of grains with Cube and Goss texture.

Combining Equation (4) and (5), with our measured results, all the constants are determined using a MATLAB calculation. The resultant equation that relates core loss to grain size, texture distribution at 1.5 T 50 HZ for our Fe-3.4 wt% Si nonoriented electrical steel, is as follows.

$$P_{1.5/50} = P_G + P_T = 3.011 + 7.604d^{-1} + 244.255d^{-2} - 0.016F_C - 0.031F_G \quad (6)$$

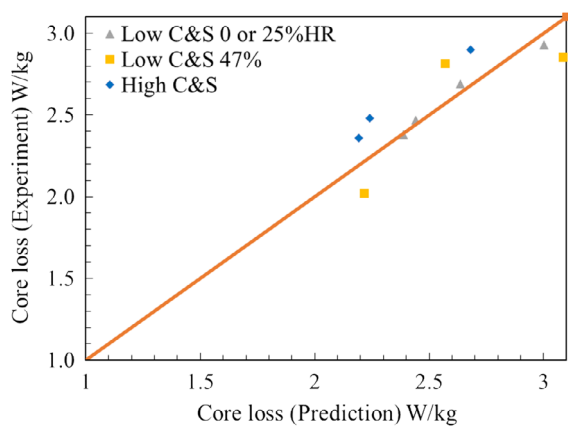


Figure 13. Comparison between predicted value and measured result on core loss $P_{1.5/50}$.

Table 3. Grain size, texture grain fraction, and magnetic properties comparison.

Group		Measured $P_{1.5/50}$ [$W\ kg^{-1}$]	Average grain size [μm]	Goss grain fraction [%]	Cube grain fraction [%]	Calculated $P_{1.5/50}$ [$W\ kg^{-1}$]
1	Low-C&S 0% HR (24 h)	2.790	136 ± 5	11.50	0.006	2.724
	Low-C&S 25% HR (6 h)	2.808	147 ± 6	9.51	0.319	2.779
2	Low-C&S 25% HR (6 h)	2.808	147 ± 6	9.51	0.319	2.779
	High-C&S 25% HR (24 h)	2.380	148 ± 6	17.50	9.400	2.381

A comparison between calculated core loss value and the measured core loss ($P_{1.5/50}$) is shown in **Figure 13**. As demonstrated in the figure, the calculated value is in reasonable agreement with the measured core loss values for a range of processing conditions. This equation separates the grain size and texture fraction's influence on core loss. To test the model, two additional groups of samples (**Table 3**) with similar average grain sizes were selected for evaluation. In group 1, a "low-C&S 25% HR (6 h)" sample with larger grain size and a lower percentage of Goss grains was used. As measured, the "low-C&S 25% HR (6 h)" sample has a higher core loss, as predicted by Equation (6). In group 2, the average grain sizes of samples are similar to each other. The "high-C&S 25% HR (24 h)" sample has a higher percentage of Goss and Cube grains and in turn has a lower calculated core loss, as predicted. The measured results are in reasonable agreement with the calculated core loss values for these samples.

Although Equation (6) separates the influence by grain size and texture, it is a simple semiempirical model and still has some limitations. For example, anomalous losses have not been considered in the calculation, and the influence of texture fraction is assumed to be linear, which still needs more theoretical study. Further research is needed to improve this calculation.

4. Conclusion

In this study, Fe-3.4 wt% Si NGO electrical steel strip samples were produced and thermomechanical processed to simulate an industrial TRSC process. With increasing annealing times at 1050 °C from 1 to 24 h, the average grain size increased, and the core loss of the fully processed samples decreased. Furthermore, the increasing annealing time also had a strong influence on the evolution of grain texture. The texture evolution in the 0% HR samples was influenced by the presence of high-intensity α^* -fiber and γ -fiber textures formed before the annealing process from the high percentage of cold reduction used in this processing path. Texture evolution can be divided into several different steps. At the initial stage of annealing, the fraction of grains smaller than critical radius decreased, but Goss grains were consumed more rapidly. Then, in the second stage of annealing, the fraction of Goss grains increased by consuming other grains. It is proposed that with the coarsening of precipitates, decreased pinning provides a mobility advantage to the surviving Goss grains which are larger than the critical size for growth. Finally, with a further decrease of

pinning force and an increase of grain size, normal grain growth is established. In this step, Cube grains can form from rotated Goss grains.

A simple model of core loss was developed to explain the influence of grain size and texture distribution on core loss. By comparing two groups of results, this equation successfully separated the influence of grain size and texture distribution on core loss.

Acknowledgements

This research was performed at Missouri University of Science and Technology (Missouri S&T). The authors would like to thank the graduate research assistants in MSE for their assistance during casting trials and acknowledge Brian Bullock for his help with the setup and manufacture of the samplers. This project was supported by Nucor Corporation and Castrip LLC, so special thanks go to all of their help and guidance. The authors are also grateful to all the faculties and industry mentoring committee of Peaslee Steel Manufacturing Research Center (PSMRC) at Missouri University of Science and Technology (Missouri S&T), for their help and guidance.

Conflict of Interest

The authors declare no conflict of interest.

Data Availability Statement

The data that support the findings of this study are available from the corresponding author upon reasonable request.

Keywords

batch annealing, electric steels, magnetic properties, textures, twin-roll strip casting

Received: April 10, 2023
Revised: September 5, 2023
Published online:

- [1] Y. Oda, T. Okubo, M. Takata, *JFE Tech. Rep.* **2016**, 21, 7.
- [2] J. Hong, H. Choi, S. Lee, J. K. Kim, Y. mo Koo, *J. Magn. Magn. Mater.* **2017**, 439, 343.
- [3] Y. Du, R. J. O'Malley, M. F. Buchely, M. Xu, in *AISTech - Iron and Steel Technology Conf. Proceedings*, **2021**, Vol. 2021-June, pp. 483–490, <https://doi.org/10.33313/382/048>.
- [4] P. Campbell, W. Blejde, R. Mahapatra, R. Wechsler, *Metallurgist* **2004**, 48, 507.
- [5] M. Sanjari, Y. He, E. J. Hilinski, S. Yue, L. A. I. Kestens, *Scr. Mater.* **2016**, 124, 179.
- [6] J. J. Sidor, K. Verbeken, E. Gomes, J. Schneider, P. R. Calvillo, L. A. I. Kestens, *Mater. Charact.* **2012**, 71, 49.
- [7] I. L. Dillamore, J. G. Roberts, A. C. Bush, *Met. Sci.* **1979**, 13, 73.
- [8] K. Murakami, N. Morishige, K. Ushioda, *Materials Science Forum*, Trans Tech Publications Ltd, Switzerland **2012**, pp. 158–163, <https://www.scientific.net/MSF.715-716.158>.
- [9] Y. Du, R. J. O'Malley, M. F. Buchely, P. Kelly, *Met. Mater. Int.* **2022**, 28, 3160.
- [10] Y. Du, R. J. O'Malley, M. F. Buchely, P. Kelly, *Appl. Phys. A* **2022**, 129, 1.
- [11] G. S. Rohrer, *Metall. Mater. Trans. B* **2010**, 41, 457.
- [12] Y. He, E. Hilinski, J. Li, *Metall. Mater. Trans. A* **2015**, 46, 5350.
- [13] M. Mehdi, Y. He, E. J. Hilinski, L. A. I. Kestens, A. Edrissy, *Acta Mater.* **2020**, 185, 540.
- [14] N. H. Fletcher, *J. Chem. Phys.* **1958**, 29, 572.
- [15] Y. Hu, H. Zhang, D. Zhao, *Spectrochim. Acta, Part A* **2021**, 250, 119376.
- [16] Y. Hayakawa, J. A. Szpunar, *Acta Mater.* **1997**, 45, 4713.
- [17] S. H. Lee, D. N. Lee, *Int. J. Mech. Sci.* **2001**, 43, 1997.
- [18] H. Jiao, Y. Xu, L. Zhao, R. D. K. Misra, Y. Tang, D. Liu, Y. Hu, M. Zhao, M. Shen, *Acta Mater.* **2020**, 199, 311.
- [19] N. Shan, J. Liu, Y. Sha, F. Zhang, L. Zuo, *Metall. Mater. Trans. A* **2019**, 50, 2486.
- [20] T. Nguyen-Minh, J. J. Sidor, R. H. Petrov, L. A. I. Kestens, *Scr. Mater.* **2012**, 67, 935.
- [21] J. Wang, Q. Ren, Y. Luo, L. Zhang, *J. Magn. Magn. Mater.* **2018**, 451, 454.